Topological Study of the Late Steps of the Artemisinin Decomposition Process: Modeling the Outcome of the Experimentally Obtained Products

Pamela Moles, Mónica Oliva, and Vicent S. Safont*

Departament de Química Física i Analítica, Universitat Jaume I, Avda. Sos Baynat s/n, 12071 Castelló, Spain

Received: July 13, 2010; Revised Manuscript Received: November 4, 2010

By using 6,7,8-trioxabicyclo[3.2.2]nonane as the artemisinin model and dihydrated $Fe(OH)_2$ as the heme model, we report a theoretical study of the late steps of the artemisinin decomposition process. The study offers two viewpoints: first, the energetic and geometric parameters are obtained and analyzed, and hence, different reaction paths have been studied. The second point of view uses the electron localization function (ELF) and the atoms in molecules (AIM) methodology, to conduct a complete topological study of such steps. The MO analysis together with the spin density description has also been used. The obtained results agree nicely with the experimental data, and a new mechanistic proposal that explains the experimentally determined outcome of deoxiartemisinin has been postulated.

Introduction

Malaria is a disease, produced by the members of the *Plasmodium* parasite gender, which spreads out mainly throughout the tropical and subtropical regions, causing more than one million deaths yearly, and especially affecting childhood.[1]

The malaria parasite enters humans through the bite of an infected Anopheles female mosquito. The mosquito inoculates motile sporozoites, which quickly arrive at the liver, where they invade hepatocytes. Six days later, the infested hepatocytes are broken, freeing tens of thousands of merozoites by each original sporozoite. The merozoites then invade the erythrocites, where they develop to mature forms (trophozoites and schizonts), releasing finally more merozoites, closing this cycle. In addition, gametocytes are also released, which can be ingested by another female Anopheles if the host is pricked again. Fertilization then takes place in the mosquito, and more sporozoites develop, which will infect a new host when the mosquito pricks another human being.[1,2]

To sustain this rapid development, the malaria parasite must synthesize its own proteins, and it obtains amino acids mainly from the digestion of the host hemoglobin.[3] However, digestion of hemoglobin also releases free heme (Fe (II) protoporphyrin-IX), which is toxic to the parasite due to its ability to destabilize and lyse membranes and inhibit the activity of some enzymes. Therefore, the parasite needs a parallel process to eliminate the toxic heme that the digestion of the host hemoglobin produces.[4,5]

At least three mechanisms have been identified by which the parasite eliminates heme: degradation facilitated by hydrogen peroxide within the parasite food vacuole, glutathione-dependent degradation in the cytoplasm of parasite, and elimination of heme by means of the formation of hemozoin or malaria pigment.[6] Some studies suggest that up to 95% of the iron arising from the digestion of the host hemoglobin is found in hemozoin, and therefore, it seems that the main mechanism of detoxification is the formation of the malaria pigment.[3,7] In this process, heme is oxidized to hemin (Fe (III) protoporphyrin-IX); then, hemin dimers (β-hematin) are formed and finally assemble to form hemozoin, an insoluble crystalline material.

There are different drugs that can be used in the malaria treatment, and many of them act by avoiding the detoxification process, therefore preventing the heme elimination. In this way, the parasite dies by accumulation of free heme. For instance, the chloroquine-derived treatments act by forming adducts with heme, avoiding in this way its polymerization to hemozoin.[8]

However, the malaria parasite has developed resistance to chloroquine-based drugs and even to quinine and mefloquine. Due to this fact, artemisinin-based combination therapies are nowadays the recommended and most used antimalarial agents.[9] They are very effective against severe malaria, caused by *Plasmodium falciparum*. Artemisinin eliminates almost all asexual forms of the parasite in its intraerythrocytic stage, preventing in this way its maturation to more pathological forms. Furthermore, artemisinin also eliminates some sexual stages, the gametocytes, avoiding in this way the disease transmission to new hosts.[9]

Artemisinin (**1**, Scheme 1) is a sesquiterpene lactone with an endoperoxide group, and its unusual 1,2,4-trioxane ring system has been proven to be essential for the antimalarial activity.[10,11] The mechanism of action of artemisinin is not clear and is still under debate.[4,12−18] However, a quite wide agreement exists in that artemisinin decomposes in the presence of heme (**2**, see Scheme 1), generating several reactive intermediates, which would be the agents directly or indirectly responsible for the malaria parasite death.[2,19]

In this context, the study of the artemisinin decomposition prompted by the presence of heme iron has a great importance in understanding the details of the antimalarial action that artemisinin and its derivatives exert.

In a recent work,[20] we have suggested that artemisinin instead of oxygen can react with heme, avoiding in this way the heme-to-hemin oxidation, with the subsequent disruption of the detoxification process. On the other hand, if artemisinin interacts with heme, the decomposition process of artemisinin takes place, and carbon-centered radicals, that are able to alquilate heme itself, are formed. In such a way, artemisinin acts in heme oxidation blocking, and as a heme alkylating agent as well. Both actions complement each other and yield the same result: the hemozoin formation is prevented, the (alkylated) heme accumulates inside the parasite, and therefore, the parasite dies.

* E-mail: safont@qfa.uji.es. Phone: 34964728085. Fax: 34964728066.

SCHEME 1
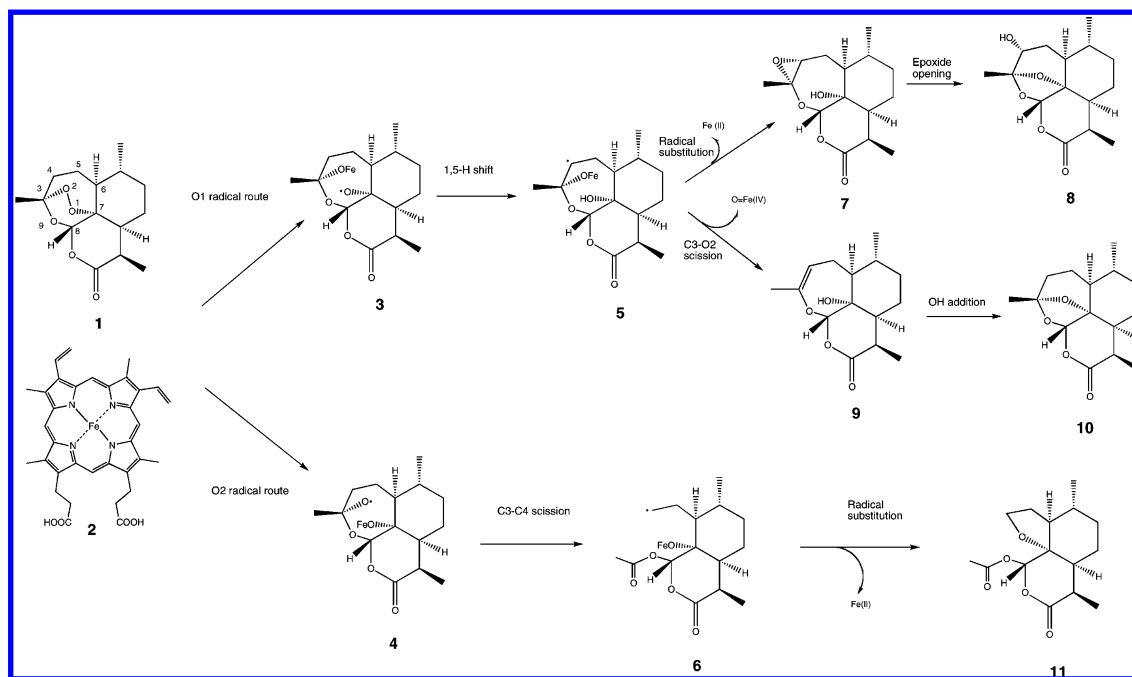
By using proper molecular models, in that work[20] the steps from the reactants initially separated (the artemisinin model and the iron complex) to the carboradicals postulated as heme alkylation agents, namely, **5** and **6** (see Scheme 1), were studied.

Experimentally, several in vitro studies demonstrate that if alkylation fails the decomposition process can continue, to render several products identified in different yields as a function of the reaction conditions.[21,22] In particular, the presence of species **8**, **10**, and **11** as products resulting from the artemisinin decomposition prompted by Fe(II) has been described. The formation of such products has been explained by means of the molecular mechanism depicted in Scheme 1.[21,23]

With the aim of completing our aforementioned study and to reveal the details of the latter stages, which can play a significant role in the thermodynamics and the kinetics of the whole artemisinin decomposition process, in the present work we describe the steps leading from the carbon-centered radicals modeling **5** and **6** to the experimentally obtained final products of the artemisinin decomposition process.

Following the same outline we used in the previous work,[20] the study has been made from two points of view: on one side, we have characterized the geometric and energetic parameters of the obtained species, and on the other side, we have conducted a topological study based on the electron localization function (ELF) and the atoms in molecules (AIM) methodology with the objective of analyzing the details concerning the electronic redistribution taking place in the processes under study. To gain a deeper insight into the electronic aspects of the studied processes, a molecular orbital (MO) analysis including the spin density description has also been done for some critical reaction steps.

Computational Methodology

Following our previous work, we have used the same simple models that allow us to perform the topological analysis and to reveal the electronic details of the studied processes. Therefore, artemisinin (**1**) has been modeled with the trioxane 6,7,8-trioxabicyclo[3.2.2]nonane (**1f**), while heme (**2**) has been modeled by dihydrated Fe(OH)$_2$ (**2f**, see Scheme 2). While the

use of **1f** to model artemisinin is well-established in the literature,[11] it is convenient to provide additional evidence that the simple **2f** model can satisfactorily represent heme in what refers to the energetic and electronic aspects studied here. To this end, we have used heme with a water molecule coordinated to the iron atom (**2**-H$_2$O) to calculate some stationary points. A comparison of the results with those obtained when using **2f** is then offered.

The aim of the present work is to characterize the stationary points in the paths from **5f** to **8f** and **10f**, and from **6f** to **11f′**, as shown in Scheme 2. The optimized structures are then characterized as minima or transition structures (TS) by means of a vibrational analysis. The transition structures have one and only one negative wavenumber, and this imaginary frequency is associated with the transition vector (TV)[24] that describes the atomic motion at TS. From each TS, the intrinsic reaction coordinate (IRC)[25] pathway to its associated minima has been calculated.

The calculations have been done by using density functional theory methods, as implemented in the *Gaussian03* package.[26] In particular, Becke's three-parameter functional[27] has been used for the exchange part and the nonlocal transformed correlation correction functional of Lee−Yang−Parr[28] for the correlation one. The 6-311+G (d,p) basis set has been applied in order to attain reliable results. The unrestricted (UB3LYP) formalism has been used, since the multiplicity is quintuplet for the global system. When using **2**-H$_2$O instead of **2f**, the 3-21G basis set has been employed for all atoms except iron, for whom the LANL2DZ scheme has been used. This combination of basis sets makes possible both to achieve reasonable calculation times and to maintain a sound description for the iron atom.

Our second goal has been to obtain a topological description of the chemical interactions characterizing these molecules and explaining the reactive processes. We have used the approach proposed by Silvi and Savin,[29] which allows a classification of chemical bonds, based on a topological analysis of the ELF gradient field. The ELF gradient field maxima are called localization attractors. These attractors can be classified into two main groups: core and valence attractors. In turn, there are

SCHEME 2
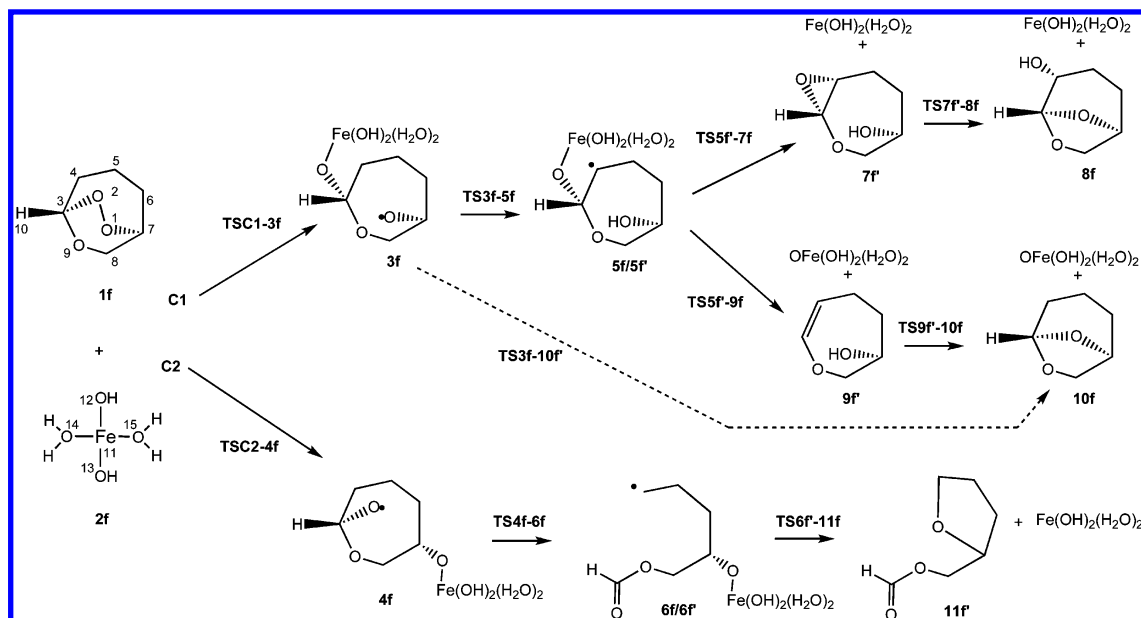
two subgroups among the valence attractors: the monosynaptic (or nonbonding) and the disynaptic (or bonding) attractors. Therefore, the molecular space can be partitioned into basins, each of them representing a region of space traversed by the trajectories of the ELF gradient field which terminate at a given attractor. ELF is interpreted as a measure of the electron localization in atomic and molecular systems, as the conditional probability of finding two paired electrons. Values above 0.5 indicate a localized character, while values below 0.5 correspond to delocalized electron density. Graphical representations are obtained by plotting isosurfaces of the localization function domains of these attractors, where an isosurface $\eta(r) = f$ encloses points for which ELF $> f$. From a quantitative point of view, the method includes integration of the electron density over the basins to obtain the basin populations.

Another electron-density-based topological analysis which provides useful information on the bond structure is the AIM theory, developed by Bader and co-workers.[30,31] With this theory, the main characteristics of the bonds which take part in each studied process have been evaluated by focusing on the properties of the corresponding bond critical points (BCP). The BCP properties we use are the charge density ($\rho(r)$), the electronic energy density ($E_d(r)$), and the Laplacian of the electron density ($\nabla^2\rho(r)$). The charge density is related to the bond strength: the higher this value is, the stronger the bond. The electronic energy density provides information about bond stability: highly negative values involve largely stable bonds. The Laplacian of the electron density values indicate concavity or convexity depending on its negative or positive value, respectively. Negative values of $\nabla^2\rho(r)$ evidence valence-shell charge concentration, while positive values mean valence-shell charge depletion. Thus, an unshared-electron (or electrostatic) interaction is characterized by low values of $\rho(r)$ and positive values of $\nabla^2\rho(r)$ in the BCP, whereas high values of $\rho(r)$ and negative values of $\nabla^2\rho(r)$ correspond to a shared-electron (or covalent) interaction.

The AIM and ELF studies have been carried out from the computed B3LYP/6-311+G(d,p) electron density, with the AIM2000[32] and TopMoD[33] software packages, respectively. ELF isosurfaces have been visualized with the AMIRA 4.1 visualization program.[34] The graphical representation of ELF has been

carried out by considering an isosurface value (*f*) of 0.815 for all structures except **5f′**, **TS5f′-9f**, **9f**, **6f′**, and **TS6f′-11f**. For these, a smaller value of 0.784 has been required to correctly visualize the basins. To visualize the monosynaptic basin associated with C4 (insets for **5f′**, see below), a value of *f* = 0.665 has been used. The color convention represents core basins in magenta, and the remaining valence basins are classified depending on their synaptic order: red for monosynaptic, green for disynaptic, and gray for hydrogenated basins. The MO analysis has also been done from the computed B3LYP/6-311+G(d,p) electron density, and GaussView 3.0[35] has been used to visualize and depict the molecular orbitals, using an isovalue of 0.05, as well as the spin density, using an isovalue of 0.001.

Results and Discussion

Experimental studies on artemisinin (**1**) decomposition reveal the formation of different species depending on the reaction conditions. By using FeSO₄ in aqueous CH₃CN, two major products (**8** and **11**) are obtained, in 67% and 25% yields, respectively, while **7** has been identified as a minor component (1−2% yield).[21] On the other hand, if the cleavage of **1** is induced by FeBr₂ in THF/1,4-cyclohexadiene, three major products are formed, namely, **10**, **11**, and **8**, in 71%, 16.7%, and 4.2% yields, respectively.[22] All the experimental observations on the artemisinin decomposition have been taken into account in the unified mechanism proposed by Cumming[23] and Wu:[21] an excerpt of such mechanism is offered in Scheme 1.

The process begins with the artemisinin endoperoxide bridge reduction mediated by Fe(II) species, like heme, thus giving rise to **3** if the mechanism takes place through O1-radical formation, or to **4** if the mechanism follows the O2-radical route. Once these O-radicals are formed, they evolve in different ways to render the indicated final products. From **3**, a 1,5-H shift leads to the C-centered radical **5**, which through several processes can attain the formation of **8** and **10**. On the other hand, **4** rearranges to the C-radical **6**, which is the precursor of the furane **11**.

In previous studies with different molecular models, we have characterized the geometries and energies of the stationary points
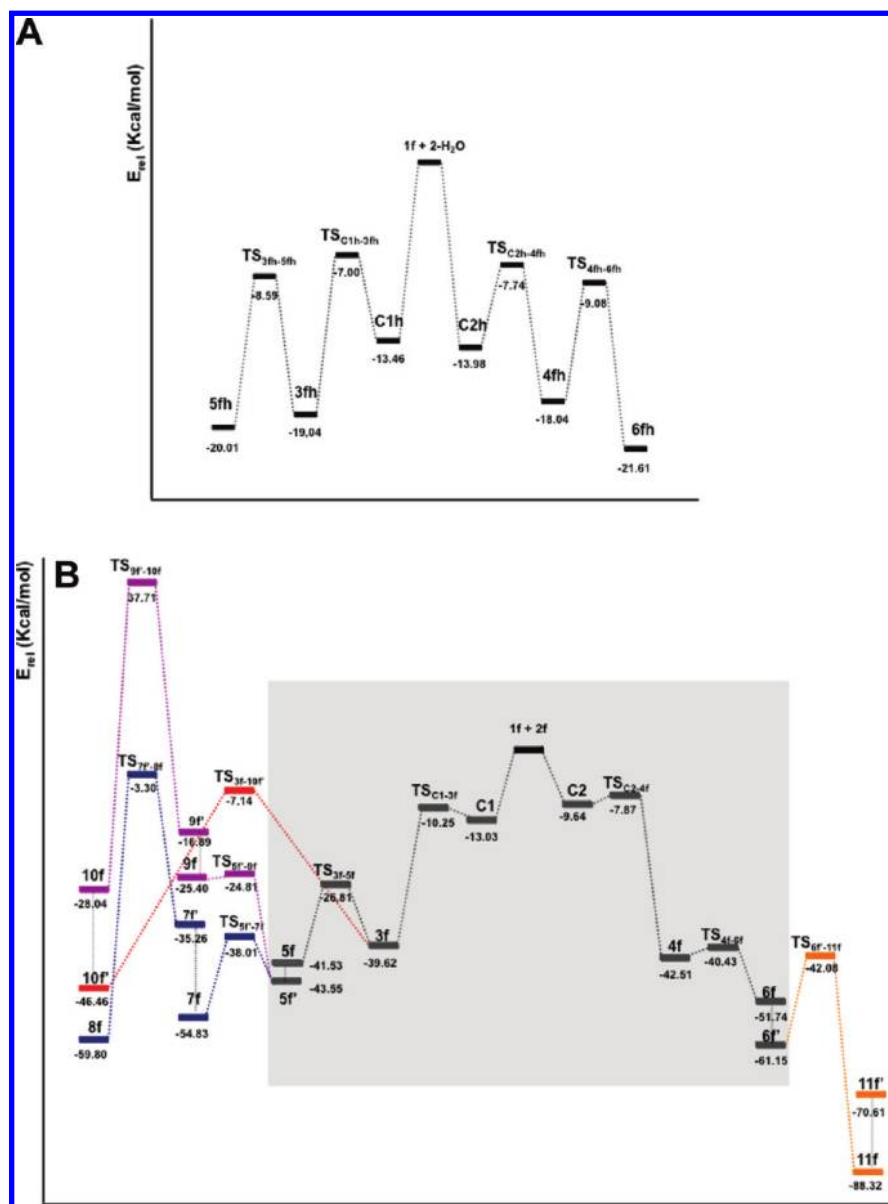
Figure 1. (a) Relative energy (kcal/mol) profile of the indicated stationary points. Total energy of the reference point (**1f** plus **2**-H_2O): -2482.023834 hartree. (b) Relative energy (kcal/mol) profile of the indicated stationary points. Total energy of the reference point (**1f** plus **2f**): -2028.772368 hartree.

involved along the potential energy surface for the whole artemisinin decomposition process.[36,37] On the other hand, using the present models, the electronic rearrangements taking place in the reaction pathway associated with the formation of the C-radicals **5f** and **6f** (see Scheme 2) have been analyzed by means of the joint use of ELF and AIM tools.[20] In the present study, we report a topological analysis of the reaction steps that lead from the C-radicals to the formation of the final products.

Previously, to establish the appropriateness of the use of **2f** to represent heme in what refers to the energetic and geometric conclusions reached, we have used **2**-H_2O and **1f** as starting molecules to calculate the reaction pathways associated with the formation of the C-radicals modeling **5** and **6**, namely, **5fh** and **6fh**. All attempts using **2**-H_2O to conduct ELF and AIM analysis have been unsuccessful. The system size prevents its use even in single topological calculations, and hence, it was not possible to make a systematic characterization of the topology of the processes herein studied.

Revisiting the First Steps of the Process: Formation of 5fh and 6fh

When **2**-H_2O approaches **1f**, two interaction complexes can be formed, namely, **C1h** and **C2h**, depending on which oxygen atom interacts with the iron atom. Both complexes are found to be more stable than the starting reactants, and from these points, two transition structures yield the O-centered radicals **3fh** and **4fh**, of similar stability to each other, and more stable than the previous complexes. The activation barriers from the interaction complexes to the corresponding transition structures (**TSC1h-3fh** and **TSC2h-4fh**) are found to be relatively small. Finally, from the O-centered radicals, two new transition structures (**TS4fh-6fh** and **TS3fh-5fh**) render the C-centered radicals **6fh** and **5fh**, respectively. Among all these stationary points, the most stable one is **6fh**, as can be seen in Figure 1a, where the energetic profile for these steps is depicted.

A comparison of the results reported above with those calculated in our previous paper[20] by using **2f** (see the gray zone

Late Steps of Artemisinin Decomposition

J. Phys. Chem. B, Vol. 115, No. 2, 2011 **337**

of Figure 1b) can now be done. The numerical values obtained differ from one model to the other. It can be noticed that the energetic differences among the minima are smaller when using **2**-H_2O. This is expected because the aromatic porphyrin cycle provides additional stability to the system, and the energetic differences from one point to another are small due to the fact that the heme moiety remains the same in all minima. On the other hand, the energetic barriers are slightly larger due to the same reason: the minima are additionally stabilized, and the conjugation is somewhat lost at the transition states. However, the main conclusions coincide by using either of the two models: the O-centered radicals are less stable than the corresponding C-centered radicals; the energies of these stationary points always lay under the energy of the starting separated species, and the most stable species is the one modeling **6**. Hence, from an energetic point of view, the use of **2f** renders the same main conclusions as the use of **2**-H_2O.

On the other hand, the main geometric parameters found are not equal, but they are rather similar to the ones obtained by using the small model,[20] and the variations in its values are analogous. Hence, following the O1 radical route, the O1−O2 distance increases from 1.55 Å at **C1h** (1.49 at **C1**) to 1.79 Å at **TSC1h-3fh** (1.66 at **TSC1-3f**), and to 4.05 Å at **3fh** (3.57 Å at **3f**), while the H−C4 distance increases from 1.10 Å at **3fh** (1.10 Å at **3f**) to 1.37 Å at **TS3fh-5fh** (1.26 Å at **TS3f-5f**) and finally to 2.50 Å at **5fh** (2.58 Å at **5f**). At the same time, the H−O1 distance shortens from 2.09 Å at **3fh** (2.21 Å at **3f**) to 1.17 Å at the TS (1.29 by using the small model) and finally to 1.02 Å at **5fh** (0.97 at **5f**).

Following the O2 radical route, the O1−O2 distance increases from 1.55 Å at **C2h** to 1.79 Å at **TSC2h-4fh** and then to 4.08 Å at **4fh**, while the C3−C4 distance increases from 1.57 Å at **4fh** to 2.06 Å at **TS4fh-6fh** and finally to 4.60 Å at **6fh**. These distances are calculated to be 1.49, 1.63, 3.27, 1.63, 1.95, and 4.25 Å, respectively, when using **2f** as molecular model. Hence, from a geometric point of view, the use of **2f** renders very similar descriptions to the use of **2**-H_2O.

O1 Radical Route: Formation of 8f

After the formation of **5f**, which is 41.53 kcal/mol more stable than the starting separated reactants **1f** and **2f** (see Figure 1b, where the energetic profile is depicted), a slight conformational change takes place leading to **5f′**, 43.55 kcal/mol below the reactants, and the nonradical molecule **8f**, that models the 3-hidroxi-deoxi-artemisinin **8**, is then formed via a two-steps mechanism. In the first step of the process, the secondary C-radical **5f′** evolves through the transition state **TS5f′-7f**, that presents a relative energy of −38.01 kcal/mol, to render the epoxide with the Fe(II)-species coordinated to the epoxide oxygen (**7f**). The relative energy of **7f** is −54.83 kcal/mol. Thereafter, the elimination of the Fe(II)-species causes a logical energy increase, due to the loss of the Fe−O interaction, from **7f** to **7f′**, that stands 35.26 kcal/mol below the starting reactants. Then, **7f′** gives rise to **8f**, whose relative energy is −59.80 kcal/mol, via the four-centered transition state **TS7f′-8f**, which presents a relative energy of −3.30 kcal/mol. As expected, **8f** is the most stable species along this reaction pathway, and all stationary points found from the starting separated reactants to the final products **8f** plus the Fe(II) complex stand below the energy of the reactants. Therefore, the **8f** formation is straightforward once the process is initiated. These results nicely explain the experimentally observed outcome of the final product modeled by **8f**, i.e., the production of **8**, in the artemisinin decomposition. In addition, the energetic profile in Figure 1b

reveals that the largest barrier to be surmounted in the pathway to **8f** is the passage through **TS7f′-8f**, and hence, it is reasonable to expect some accumulation of the previous intermediate, i.e., of **7f′**. This is experimentally confirmed by the detection of **7** in some experiments in small quantities.[21]

The geometric changes taking place in the first step of the reaction involve the O2 and C4 atoms that approach each other until the epoxide **7f** is formed (see Figure 2). The distance between these atoms is 2.37 Å in **5f′**, 2.03 Å in **TS5f′-7f**, and 1.49 Å in **7f**. Simultaneously, the O2−Fe bond breaks, showing distances of 1.84 Å, 1.96 Å, and 2.23 Å at **5f′**, **TS5f′-7f**, and **7f**, respectively. In the second step, **7f′** gives rise to **8f**, and four bonds participate in the reaction: the hydrogen atom moves from O1 to O2, and its distance to O1 varies from 0.97 Å in **7f′** to 1.20 Å and 2.34 Å at **TS7f′-8f** and **8f**, respectively. The H approaching O2 to form another alcohol group can be noted by the H distance to O2 that evolves from 2.14 Å in **7f′** to 1.23 Å in the transition structure and finally to 0.97 Å at the product **8f**. In addition, the distance between O2 and C3 enlarges as the reaction advances, being 1.44 Å at **7f′**, then 2.24 Å at **TS7f′-8f**, and finally 2.41 Å at **8f**. At the same time, a bond between O1 and C3 is formed as the reaction proceeds: the distances are 3.35 Å, 2.53 Å, and 1.42 Å going from the reactants to the product, through the transition state.

The ELF study of this reaction provides information about the electronic rearrangements that take place until **8f** is formed (see Figure 3a,b). The radical **5f′** presents a monosynaptic basin populated with 0.34 electrons in C4 (see the inset in Figure 3a), thus giving support to the C-radical character of the molecule. This basin disappears from **TS5f′-7f** on, because the rest of the molecules until **8f** do not have unpaired electrons on the carbon atom. In **5f′**, there is a disynaptic basin between Fe and O2 with a population of 6.21 electrons, showing the bond between these atoms. In **TS5f′-7f**, two dysinaptic basins with populations of 2.84 and 3.24 electrons are located between these core atoms, showing the diminution of the bond strength. In **7f**, there is a dysinaptic basin of 2.65 electrons between these atoms and a monosynaptic basin of 2.74 electrons located in O2, reflecting a further diminution of the bond strength. In this structure, there is a disynaptic basin between O2 and C4 with a population of 0.91 electrons that represents the epoxide formed by O2.

In the second step of the reaction (Figure 3b), **7f′** shows a disynaptic basin of 1.09 electrons between O2 and C3, which is not present in **TS7f′-8f** and **8f** due to the bond scission. The hydrogenated basin next to the O1 core atom has a population of 1.75 electrons in **7f′** and becomes much less populated (0.38 electrons) in the transition state, where it is located between O1 and O2. This can be explained because the hydrogen is midway between the donor and the acceptor atoms, and the oxygen atoms withdraw the hydrogen electron density. In **8f**, this basin is populated with 1.74 electrons and belongs to O2, while a disynaptic basin of 1.35 electrons appears between O1 and C3.

On the other hand, the MO analysis and the spin density description provide direct evidence for the location of the radicals during the reaction steps, and therefore reveal the physical background for the reaction mechanisms (see Figure 4a,c,d). As can be seen from Figure 4a, the spin density at **5f′** accumulates mainly at the C4 and at the iron atom and its coordination sphere. This is what can be expected because the molecule is a C4-radical. Furthermore, the HOMO is centered at C4, confirming that the unpaired electron will be associated to this atom and would occupy the HOMO. As further evidence
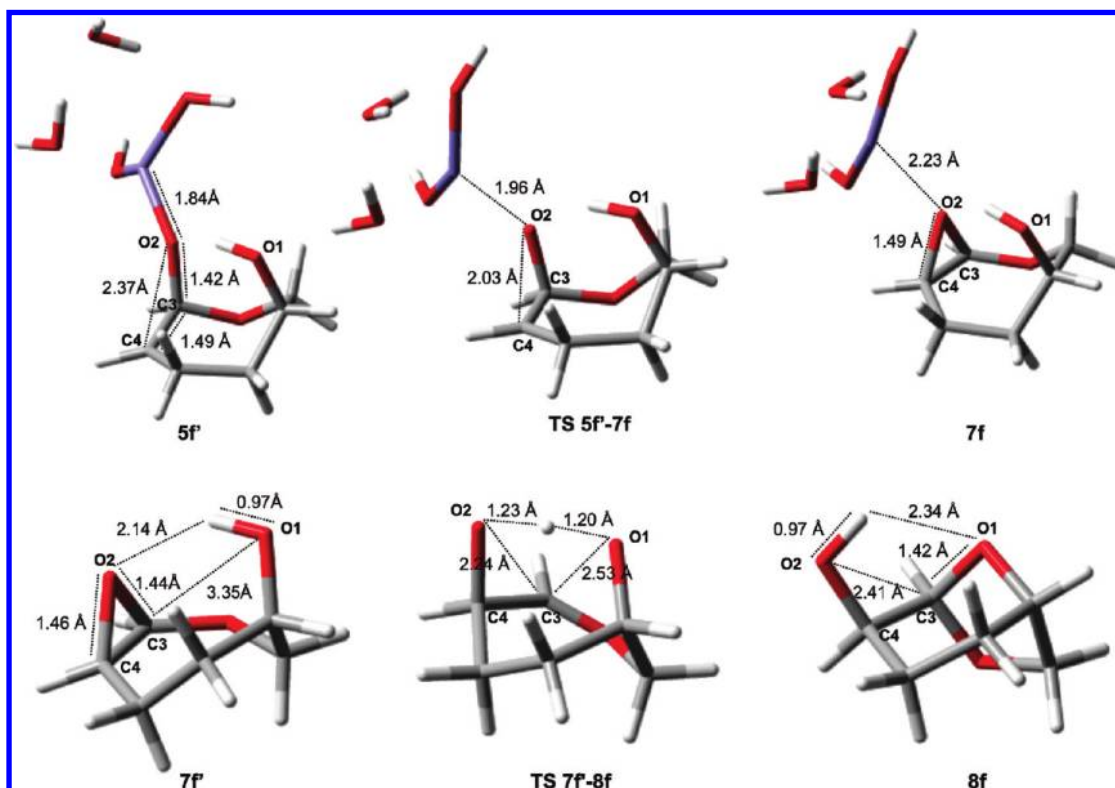
Figure 2. Structures of the indicated stationary points. Selected distances (angstroms) are included.

of the appropriateness of using the **2f** modeling heme, we also depict the spin density and the HOMO of **5fh** in Figure 4b. As can be seen, the spin density accumulates at C4 and at the Fe atom, and the HOMO is mainly associated with the unpaired electron at C4. Hence, the conclusions are the same whatever the model.

At the **TS 5f'-7f**, the spin density and the HOMO exhibit a very similar shape to **5f'**: both are still mainly associated with the unpaired electron at C4. From these data, it can be concluded that the TS has an early character. This is confirmed by the AIM analysis of the O2–C4 BCP (see below).

The AIM theory is a helpful tool to analyze the main characteristics of the bonds of each reaction step by examining the properties of the BCPs (Table 1). The epoxide **7f** formation from the C-radical **5f'** can be explained by O2–Fe bond cleavage and O2–C4 bond formation. The BCP found between O2 and Fe atoms in **5f'** has a $\rho(r)$ of 0.123 au, while for **TS5f'-7f**, this value decreases to 0.087 au and to 0.044 au in **7f**. $E_d(r)$ for this BCP shows negative values of −0.027 au in **5f'** and −0.007 au in the transition state and the positive value of 0.001 au in **7f**. The $\nabla^2\rho(r)$ for this BCP is positive for the three structures, so it is located in a charge depletion region, although it becomes less positive when going from **5f'** to **7f**, showing a value of 0.659 au in **5f'**, 0.504 au in the transition state, and 0.233 au in **7f**. These parameters demonstrate that the O2–Fe bond is not very strong and has an ionic character in **5f'**, and confirm that the Fe atom is weakly complexed to O2 in **7f**. Regarding the O2–C4 reaction coordinate, no BCP has been found between these atoms either in **5f'** or in **TS5f'-7f**, while it appears in **7f** with a value of 0.214 au for $\rho(r)$, −0.217 au for $E_d(r)$, and −0.154 au for $\nabla^2\rho(r)$, which gives support to the bond formation and reveals that the TS has early character with respect to this bond formation, in agreement with the large O2–C4 distance (2.03 Å) at the TS.

In **7f'**, a BCP between O2 and C3 atoms has been located, with a $\rho(r)$ of 0.248 au, an $E_d(r)$ of −0.292 au and a $\nabla^2\rho(r)$ of

−0.374 au, showing that the epoxide is formed. In **TS7f'-8f** and **8f**, the BCP between these atoms does not appear, because the epoxide bond opens. In accordance with this, as can be seen in Figure 2, the corresponding C3–O2 distance is 2.24 Å at the TS. The BCP found between O1 and H, shows that the alcohol bond is formed in **7f'**, as the properties of the BCP confirm: $\rho(r)$ is 0.361 au, $E_d(r)$ is −0.697 au, and $\nabla^2\rho(r)$ is −2.502 au. In **TS7f'-8f**, this bond becomes weaker: its corresponding BCP has a $\rho(r)$ of 0.179 au, an $E_d(r)$ of −0.172 au, and a $\nabla^2\rho(r)$ of −0.310 au, and in **8f**, this bond does not exist, since no BCP has been found between O1 and H. A hydrogen bond between O2 and this H can be sensed at **7f'**, and hence, a BCP is found between these atoms, with values of 0.018 au for $\rho(r)$, 0.001 au for $E_d(r)$, and 0.060 au for $\nabla^2\rho(r)$. In **TS7f'-8f**, this interaction becomes slightly stronger, with values of 0.167 au for $\rho(r)$, −0.145 au for $E_d(r)$, and −0.207 au for $\nabla^2\rho(r)$, whereas in **8f**, the O2–H bond is formed, as the BCP properties indicate, with values of 0.364 au for $\rho(r)$, −0.696 au for $E_d(r)$, and −2.490 au for $\nabla^2\rho(r)$. In **TS7f'-8f**, a BCP between O1 and C3 has been found, describing a very weak interaction, with values of 0.025 au for $\rho(r)$, 0.001 au for $E_d(r)$, and 0.075 au for $\nabla^2\rho(r)$, in accordance with the very long distance of 2.53 Å. In **8f**, this BCP shows values of 0.264 au for $\rho(r)$, −0.343 au for $E_d(r)$, and −0.584 au for $\nabla^2\rho(r)$, resulting in a stable bond.

O1 Radical Route: Formation of 10f

Another two-step mechanism from the C-radical **5f'** can give rise to the final product **10f**, which is a model of the deoxiartemisinin **10**, a compound experimentally obtained in the artemisinin decomposition.[22] The first step leads to the species **9f**, with a relative energy of −25.40 kcal/mol, via the **TS5f'-9f** that has a relative energy of −24.81 kcal/mol (see Figure 1b). This step is less favorable than the previously explained formation of **7f**, both from a thermodynamic and a kinetic point of view. From **9f**, the elimination of the Fe(IV)
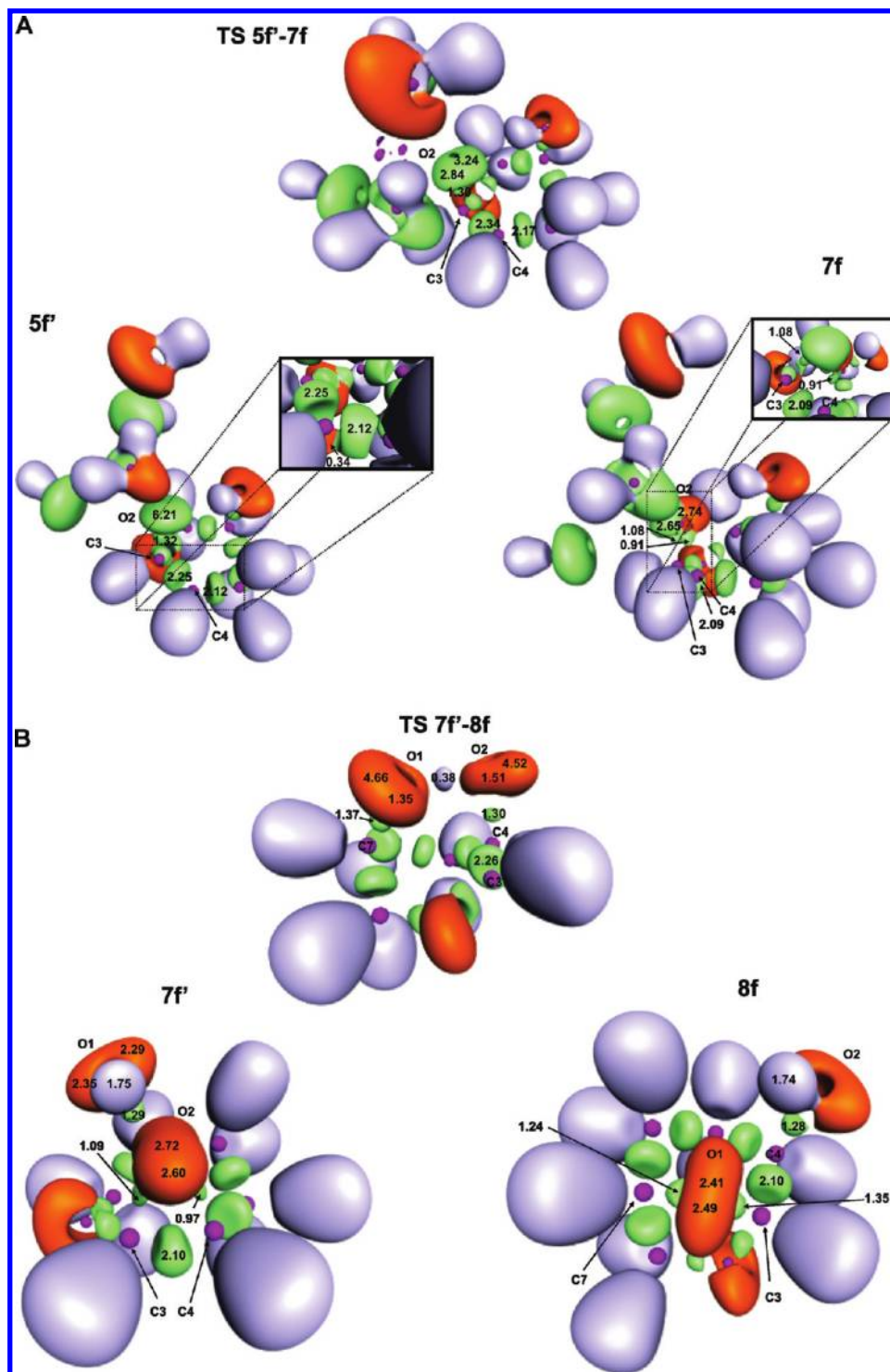
Late Steps of Artemisinin Decomposition

J. Phys. Chem. B, Vol. 115, No. 2, 2011 **339**

Figure 3. (a) ELF isosurfaces for **5f′**, **TS5f′-7f**, and **7f**. (b) ELF isosurfaces for **7f′**, **TS7f′-8f**, and **8f**.

species can give **9f′**, and the sum of the energies of **9f′** and the $OFe(OH)_2(H_2O)_2$ species stands 16.89 kcal/mol below the reactants. In the second reaction step, the four-centered **TS9f′-10f**, 37.71 kcal/mol less stable than the starting reactants, precedes the final product **10f**, whose relative energy is −28.04 kcal/mol. From these values, it can be concluded that the path leading to **10**, as proposed in the bibliography, is very unfavorable, mostly if compared with the path leading to **8**, and it is very difficult to explain how **10** can be obtained as the main product of artemisinin decomposition in some cases.[22] Furthermore, due to the high energy barrier calculated going from **9f′** to **10f**, some accumulation of intermediate **9f′**, that

models the alquene **9** (see Scheme 1), should be expected. However, to the best of our knowledge the experimental detection of **9** in the artemisinin decomposition experiments has never been reported.

Therefore, we have explored a mechanistic alternative: a direct Fe(IV)-species elimination from **3f**, to render **10f**. In this way, we have found a transition structure that opens a new mechanistic route, not proposed before, to the formation of **10**. The **TS3f-10f′** lays 7.14 kcal/mol below the starting separated reactants, and from this point, the species **10f′**, 46.46 kcal/mol under the energy of the reactants, can be found. The species **10f′** corresponds to **10f** complexed with the Fe(IV) species, with
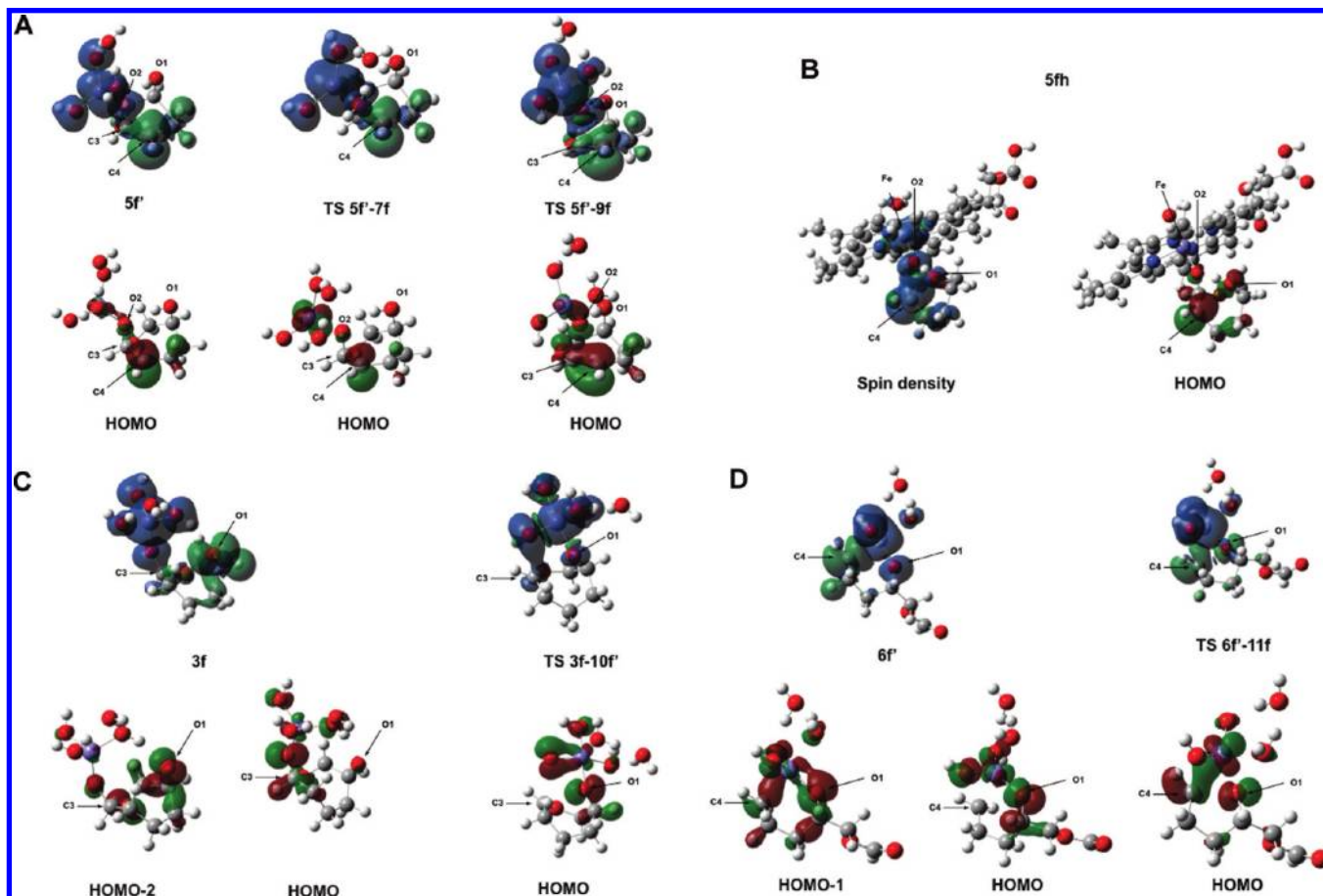
Figure 4. (a) Upper row: spin density of the indicated stationary points; the green regions correspond to negative spin density while blue zones correspond to positive spin density. Lower row: selected molecular orbitals of the indicated stationary points. (b) Spin density and HOMO of **5fh**. (c) Upper row: spin density of the indicated stationary points. Lower row: selected molecular orbitals of the indicated stationary points. (d) Upper row: spin density of the indicated stationary points. Lower row: selected molecular orbitals of the indicated stationary points.

a strong interaction between the Fe and the O1 atoms. The Fe(IV) species departure produces an energy increase to finally obtain **10f**. It should be pointed out that all the stationary points found in this new pathway lay under the energy level of the starting reactants, and hence, the product formation is again straightforward once the process is initiated. This alternative path would avoid the passage through the species modeling **9**, and this would explain why such a species has never been experimentally identified. Furthermore, it should be noted that the **TS3f-10f′** has an energy value very similar to that of the **TS7f′-8f**. This fact suggests some competition between the pathway leading to **10** and the pathway leading to **8**, and in fact from the experimental data, it is deduced that the predominant formation of one product or another depends mainly on the experimental conditions.

As indicated above, the path proposed in the bibliography to explain the appearance of **10** starts from **5** and involves O2−C3 scission, with C3−C4 double bond formation and Fe(IV) species departure (see Figure 5a). The O2−C3 distance is 1.42 Å in **5f′**, and evolves to 2.09 Å in **TS5f′-9f** and 2.44 Å in **9f**, where the dihydrated O=Fe(IV)(OH)$_2$ stays complexed with the alquene. On the other hand, the C3−C4 distance shortens from 1.49 Å in **5f′** to 1.39 Å in **TS5f′-9f** and 1.37 Å in **9f**. In the second step, the O1−H distance increases as the reaction advances, from 0.96 Å in **9f′**, to 1.83 Å in **TS9f′-10f**, and 2.64 Å in **10f**. At the same time, O1−C3 and H−C4 distances shorten with the process, being 2.68 Å and 1.14 Å, respectively, at **TS9f′-10f** and 1.42 Å and 1.10 Å, respectively, at **10f**. Moreover,

the C3−C4 bond evolves from double to single, and hence, this distance is 1.34 Å in **9f′**, 1.45 Å at the transition state, and 1.53 Å in **10f**.

The study of the ELF evolution is presented in Figure 6a,b for the path proposed in the bibliography. As can be seen, **5f′** has a disynaptic basin between O2 and C3 populated with 1.32 electrons, which disappears in **TS5f′-9f** and **9f** as a consequence of the O2−C3 bond scission. The disynaptic basin found between O2 and Fe has a population of 6.21 electrons in **5f′**, and it increases to 7.14 electrons in the transition state and 7.13 in **9f**, thus reflecting the electron transfer to the iron atom from the O2−C3 cleavage. The disynaptic basin located between C3 and C4 has 2.25 electrons in **5f′** and increases in the transition state and **9f** to 3.06 and 3.19 electrons, respectively, due to the formation of the double bond. Precisely the formation of the C3−C4 double bond is the main feature of the HOMO at **TS5f′-9f**, as can be seen in Figure 4a. The spin density that has been found to accumulate on C4 at **5f′**, is slightly delocalized from C4 to C3 at the TS, showing that the double bond begins to be formed, in agreement with the ELF and AIM (see below) results.

In the second step (Figure 6b), the hydrogen transfer from O1 to C4 is reflected by the evolution of the hydrogenated basin found next to O1 in **9f′** and populated with 1.73 electrons. As can be seen, this basin increases its population to 1.87 electrons and is placed between O1 and C4, at **TS9f′-10f**, while at **10f**, it is located next to C4 with a population of 2.02 electrons. Although in **9f′** and **TS9f′-10f** there is not a disynaptic basin between O1 and C3, it appears at **10f** with a population of 1.36

Late Steps of Artemisinin Decomposition

J. Phys. Chem. B, Vol. 115, No. 2, 2011 **341**

TABLE 1: Electronic Properties for the Bond Critical Points (BCP) Participating in the Reactions[a]

	bond	$\rho(r)$	$\nabla^2\rho(r)$	$E_d(r)$
	O2-C4	-	-	-
5f'	O2-Fe	0.123	0.659	-0.027
	O2-C3	0.262	-0.551	-0.342
	C3-C4	0.267	-0.660	-0.230
TS 5f'-7f	O2-C4	-	-	-
	O2-Fe	0.087	0.504	-0.007
7f	O2-C4	0.214	-0.154	-0.217
	O2-Fe	0.044	0.233	0.001
7f'	O2-C3	0.248	-0.374	-0.292
	O1-H	0.361	-2.502	-0.697
	O2-H	0.018	0.060	0.001
	O1-C3	-	-	-
TS7f'-8f	O2-C3	-	-	-
	O1-H	0.179	-0.310	-0.172
	O2-H	0.167	-0.207	-0.145
	O1-C3	0.025	0.075	0.001
8f	O2-C3	-	-	-
	O1-H	-	-	-
	O2-H	0.364	-2.490	-0.696
	O1-C3	0.264	-0.584	-0.343
TS 5f'-9f	O2-C3	0.056	0.149	-0.003
	C3-C4	0.313	-0.879	-0.325

	bond	$\rho(r)$	$\nabla^2\rho(r)$	$E_d(r)$
9f	O2-C3	-	-	-
	C3-C4	0.322	-0.922	-0.347
9f'	C3-C4	0.340	-0.993	-0.389
	O1-H	0.366	-2.476	-0.694
	O1-C3	-	-	-
	C4-H	-	-	-
TS 9f'-10f	C3-C4	0.281	-0.738	-0.274
	O1-H	0.041	0.132	0.000
	O1-C3	-	-	-
	C4-H	0.246	-0.753	-0.224
	C3-O2	0.286	-0.471	-0.406
3f	O1-C3	-	-	-
	Fe-O1	-	-	-
	Fe-O2	0.118	0.687	-0.023
	C3-O2	0.027	0.090	0.002
TS 3f-10f'	O1-C3	0.028	0.086	0.000
	Fe-O1	0.103	0.493	-0.015
	Fe-O2	0.206	0.780	-0.113
	C3-O2	-	-	-
10f'	O1-C3	0.243	-0.475	-0.302
	Fe-O1	0.054	0.272	0.001
	Fe-O2	0.223	0.829	-0.135

	bond	$\rho(r)$	$\nabla^2\rho(r)$	$E_d(r)$
	C3-C4	0.252	-0.595	-0.205
10f	O1-H	-	-	-
	O1-C3	0.267	-0.606	-0.348
	C4-H	0.274	-0.907	-0.270
6f'	O1-Fe	0.130	0.654	-0.032
	C4-O1	-	-	-
TS 6f'-11f	O1-Fe	0.082	0.422	-0.006
	C4-O1	0.071	0.129	-0.010
11f	O1-Fe	0.047	0.256	0.001
	C4-O1	0.231	-0.358	-0.285
11f'	C4-O1	0.249	-0.470	-0.317

[a] Electron density, $\rho(r)$ (atomic units), laplacian of the electron density, $\nabla^2\rho(r)$ (atomic units), and electronic energy density, $E_d(r)$ (atomic units).

electrons, due to the O1-C3 bond formation. On the other hand, the C3-C4 bond evolves from double, at **9f'**, to single bond along the reaction path to **10f**, and this can be sensed by following the evolution of the disynaptic basin between these atoms. The sum of the populations of the two disynaptic basins

(for the double bond) found between C3 and C4 at **9f'** is 3.68 electrons, and decreases to 2.30 and 2.02 electrons in **TS9f'-10f** and **10f**, respectively, where only one basin is found between these atoms.

By using the AIM theory (see Table 1), it has been found that the BCP located between O2 and C3 atoms has a $\rho(r)$ of 0.262 au in **5f'** and of 0.056 au in **TS5f'-9f**, while the corresponding BCP has not been found in **9f**, since the bond has been completely broken. The bond scission can be explained also by the $E_d(r)$ of this BCP, with a value of -0.342 au in **5f'** and -0.003 au in **TS5f'-9f**, as well as by $\nabla^2\rho(r)$, which shows that the BCP is located in a charge accumulation region in **5f'** (-0.551 au) and in a charge depletion zone in **TS5f'-9f** (0.149 au). On the other hand, the increase of the C3-C4 bond strength is shown by increasing the $\rho(r)$ value, and the increase of the negative values of $\nabla^2\rho(r)$ and $E_d(r)$, when going from **5f'** to **9f** (see the values in Table 1).

As for the second step of the process, in **9f'** a BCP between O1 and H is found, whose properties show that the alcohol bond is formed: $\rho(r)$ is 0.366 au, $E_d(r)$ is -0.694 au, and $\nabla^2\rho(r)$ is -2.476 au. In **TS9f'-10f**, this BCP has a $\rho(r)$ of 0.041 au, an $E_d(r)$ of 0.000 au, and a $\nabla^2\rho(r)$ value of 0.132 au, thus reflecting that the alcohol bond is being broken. In **10f**, the corresponding BCP does not exist, because the O1-H bond has disappeared. On the other hand, the BCP located between C3 and C4, which corresponded to a double bond in **9f'**, shows that the bond is weaker at **TS9f'-10f**, because $\rho(r)$ is lower than at **9f'**, and $E_d(r)$ and $\nabla^2\rho(r)$ are less negative. Finally, at **10f** this bond is simple and the corresponding values are 0.252 au for $\rho(r)$, -0.205 au for $E_d(r)$, and -0.595 au for $\nabla^2\rho(r)$.

In **TS9f'-10f**, there is a BCP between C4 and the H which is being transferred from O1 to C4, with values of 0.246 au for $\rho(r)$, -0.224 for $E_d(r)$, and -0.753 au for $\nabla^2\rho(r)$. This BCP shows that the bond is formed at **10f**, as indicated by the values of 0.274 au for $\rho(r)$, -0.270 au for $E_d(r)$, and -0.907 au for $\nabla^2\rho(r)$. A comparison of the values between **TS9f'-10f** and **10f** makes apparent the late character of the TS, in what refers to this bond, as can also be noted by the short C4-H distance of 1.14 Å. However, the TS can be described as asynchronous, because the O1-C3 distance is long, in accordance with the lack of a BCP between these atoms, and hence, the TS has an early character in what refers to the O1-C3 bond. In **10f**, the BCP between O1 and C3 does appear, representing the bond formation. The $\rho(r)$ value is 0.267 au, the $E_d(r)$ value is -0.348 au, and the $\nabla^2\rho(r)$ value is -0.606 au.

The direct path proposed here linking **3f** with **10f** is depicted in Figure 5b. As can be seen, the O1 atom approaches C3 as the reaction takes place: the distance evolves from 3.49 Å at **3f** to the final value of 1.42 Å at **10f**. At the transition structure, the distance is 2.45 Å, and at **10f'**, the corresponding value is 1.45 Å. At the same time, the O2-C3 distance enlarges from 1.38 Å at **3f** to 3.13 Å at **10f'** because this bond breaks. Interestingly, the Fe atom, initially linked to O2 by a distance of 1.83 Å, and far from O1 (at 3.97 Å distance) approaches the latter oxygen atom, and a distance of 1.91 Å between Fe and O1 is obtained at the TS. The Fe(IV) species then departs, while the bicyclic structure **10f** closes, although at **10f'**, there is still a strong interaction between Fe and O1.

The ELF analysis is depicted in Figure 6c. As can be seen, in **3f** there is a disynaptic basin between O2 and C3 populated with 1.36 electrons, showing that these atoms are bonded. In **TS3f-10f'** and in **10f'**, there is no basin between these atoms, which evidences the bond cleavage. The O1-C3 bond formation becomes obvious in the product **10f'**, because a disynaptic basin
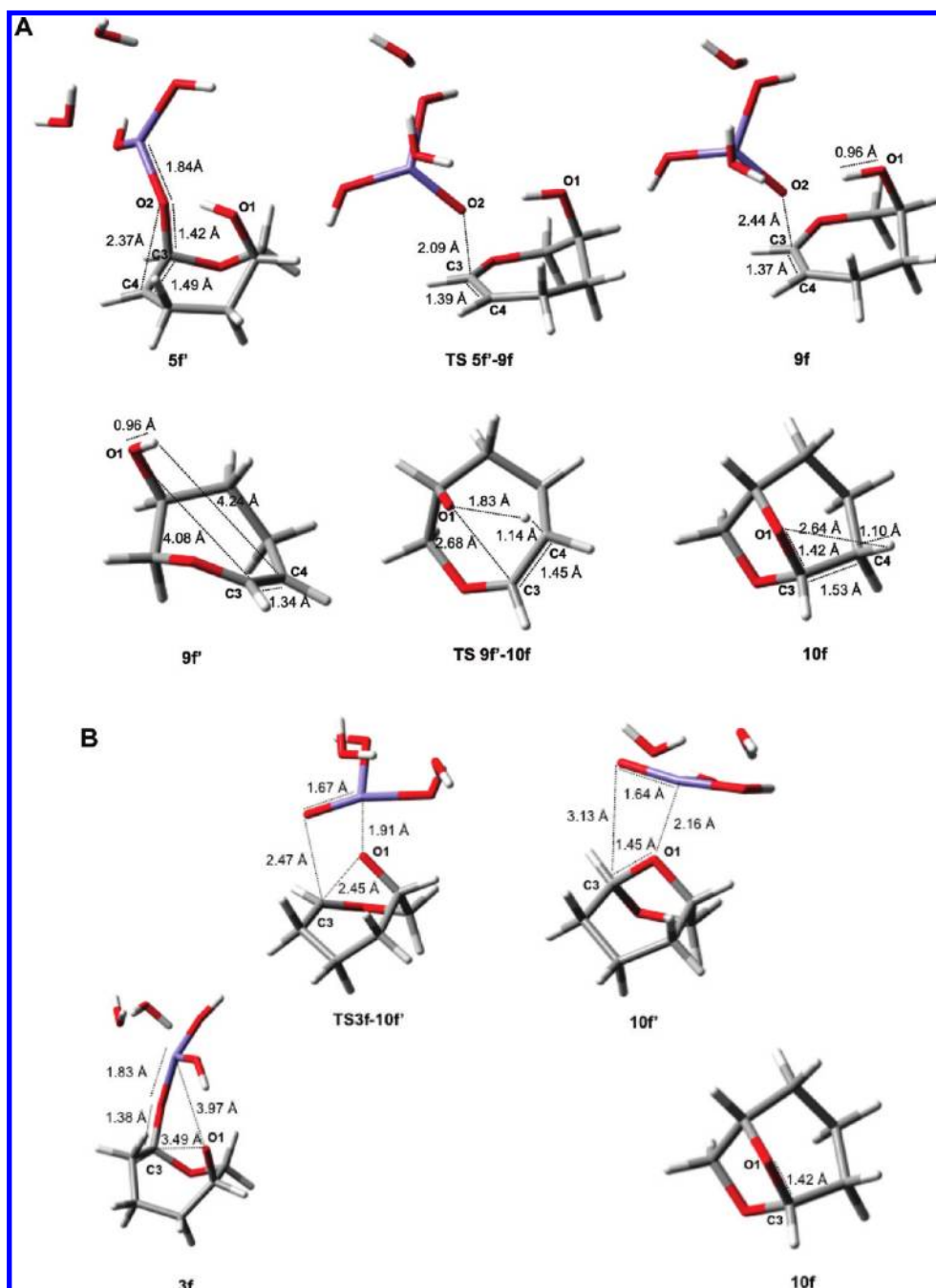
Figure 5. (a) Structures of the indicated stationary points. Selected distances (angstroms) are included. (b) Structures of the indicated stationary points. Selected distances (angstroms) are included.

with 1.33 electrons in the population appears in this structure. Nevertheless, in **3f** and **TS3f-10f′** this basin does not exist. In **3f**, the disynaptic basin between Fe and O2 has a population of 6.14 electrons, and in the **TS3f-10f′**, the population of the basins between Fe and O2 increases to a total value of 6.87 electrons. Since the Fe locates between both oxygen atoms (O1 and O2) in the transition state, a disynaptic basin of 1.35 electrons between O1 and Fe appears. In **10f′**, the basin between Fe and O2 has a bigger population (7.04 electrons) attributed to the Fe—O2 double bond formation. In **10f′**, the Fe atom stays coordinated to O1, but there is no basin between them, and O1 shows two unshared basins populated with 2.57 and 2.34 electrons in each one.

The spin density, depicted in Figure 4c, accumulates on O1 at **3f**, showing its O-radical character. At the TS, however, very little spin density remains on O1 because, as stated above, the

Fe atom strongly interacts with O1, which, at the same time, approaches C3 to form the O1—C3 bond. It can be seen that the HOMO at the TS is associated with the Fe—O2 double bond formation, with some participation of O1 p-type orbital. At the O-radical **3f**, the unpaired electron on O1 occupies the HOMO-2 orbital, while the HOMO is related with some C3—O2 anti-bonding interaction that would facilitate the breaking of this bond.

The AIM study of this reaction step also describes the same tendencies as the ELF, since in **3f**, there is a BCP between C3 and O2 atoms whose $\rho(r)$ is 0.286 au, while in **TS3f-10f′**, this value decreases to 0.027 au and the BCP does not appear in **10f′**, because the bond is broken in this structure. The bond is more stable in **3f** than in **TS3f-10f′**, as is shown by the values of -0.406 au and 0.002 au for $E_d(r)$, respectively. The $\nabla^2\rho(r)$ of this BCP is negative at **3f**, so it is located in a charge
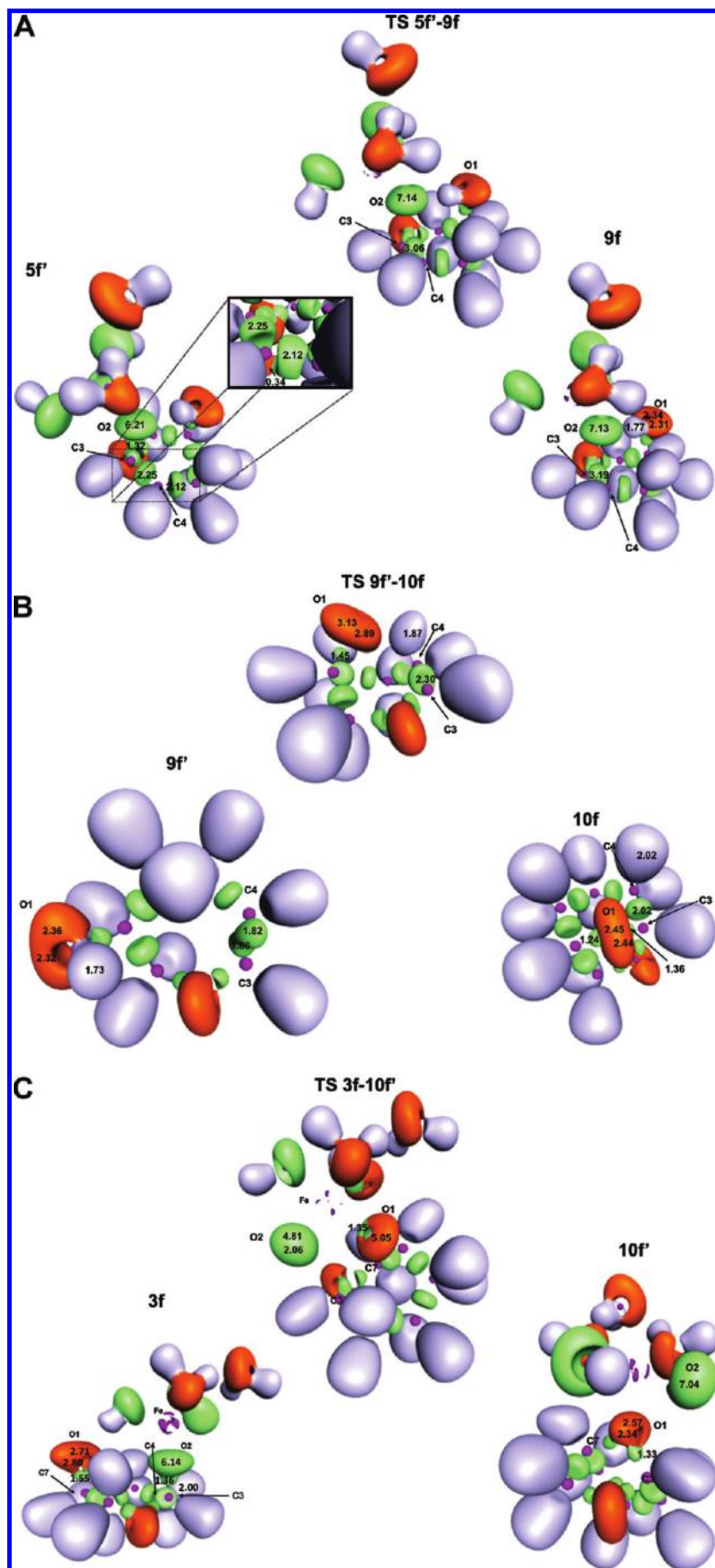
Late Steps of Artemisinin Decomposition

J. Phys. Chem. B, Vol. 115, No. 2, 2011 **343**

Figure 6. (a) ELF isosurfaces for **5f′**, **TS5f′-9f**, and **9f**. (b) ELF isosurfaces for **9f′**, **TS9f′-10f**, and **10f**. (c) ELF isosurfaces for **3f**, **TS3f-10f′**, and **10f′**.
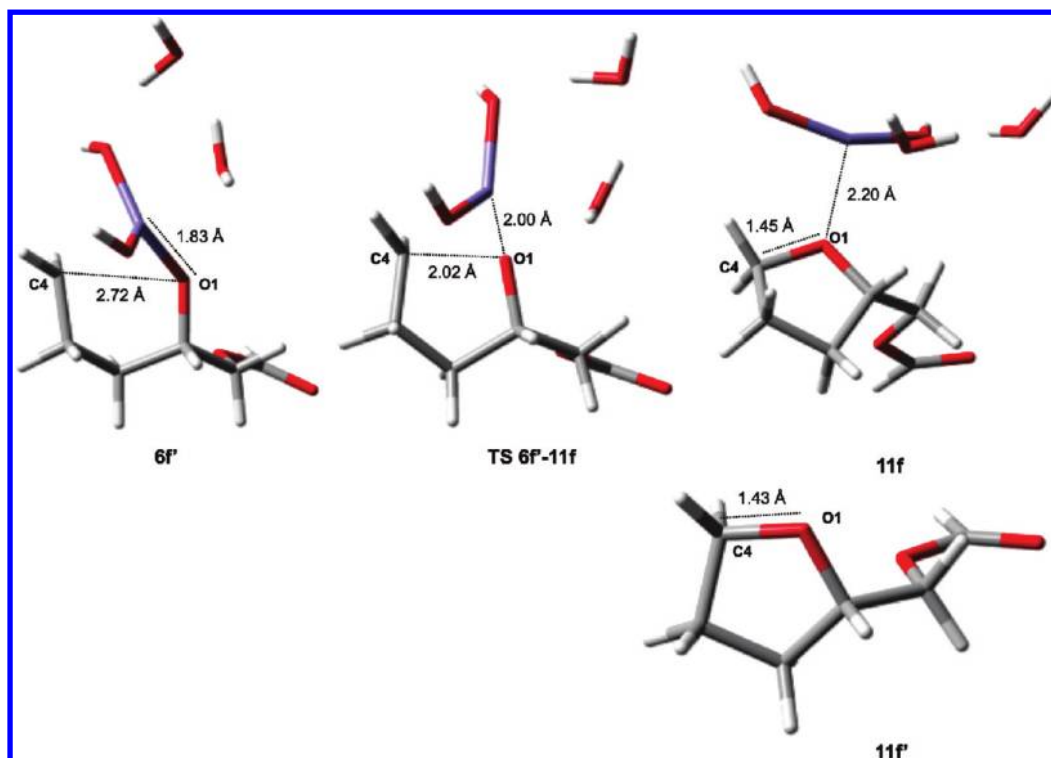
Figure 7. Structures of the indicated stationary points. Selected distances (angstroms) are included.

concentration region, while at **TS3f-10f′**, it is positive and located in a charge depletion region. The O1−C3 bond is very weak in **TS3f-10f′**, as the small value of $\rho(r)$ (0.028 au), the null value of $E_d(r)$, and the positive value of $\nabla^2\rho(r)$ (0.086 au) show. The formation of this bond is demonstrated by the BCP which exists in the product **10f′** with a $\rho(r)$ value of 0.243 au, a negative $E_d(r)$ of −0.302 au, and a $\nabla^2\rho(r)$ located in a charge concentration region with a value of −0.475 au. This BCP is not present at **3f**. The BCP located between O2 and Fe has a $\rho(r)$ of 0.118 au in **3f** and increases to 0.206 au in **TS3f-10f′** and to 0.223 au in **10f′**, as it evolves from single to double bond character. $E_d(r)$ of this BCP shows the same trend, as its values are −0.023 au, −0.113 au, and −0.135 au at **3f**, **TS3f-10f′**, and **10f′**, respectively. The $\nabla^2\rho(r)$ parameter of this BCP has positive values for the three structures (0.687 au for **3f**, 0.780 au for **TS3f-10f′**, and 0.829 au for **10f′**), it is located in a charge depletion region in all cases, but the bigger value in **10f′** shows that the O−Fe bond formed has ionic character. To achieve the suitable geometry to go from **3f** to **10f′**, a BCP between O1 and Fe appears in the **TS3f-10f′**, with a $\rho(r)$ of 0.103 au, an $E_d(r)$ of −0.015 au, and a $\nabla^2\rho(r)$ of 0.493 au. In **10f′**, the values of this BCP show the Fe is coordinated to O1 more weakly, as it has a $\rho(r)$ of 0.054 au, a $E_d(r)$ of 0.001 au, and a $\nabla^2\rho(r)$ of 0.272 au.

O2 Radical Route: Formation of 11f

The O2-radical route leads to the formation of the C-radical **6**, which is the precursor of the product **11**, the experimentally characterized ring contracted THF-acetate.[21,22] We have modeled the reaction with a previous step, in which **6f**, whose relative energy is −51.74 kcal/mol, renders **6f′** by means of a conformational change (see Figure 1b). The last species lays 61.15 kcal/mol below the starting reactants. From this point, **11f** is found 88.32 kcal/mol more stable than the reference starting reactants. The mechanism involves the four-centered transition state **TS6f′-11f**, whose relative energy is −42.08 kcal/mol.

Finally, the Fe(II) species release renders **11f′**, and the sum of the energies of **11f′** and the Fe(OH)$_2$(H$_2$O)$_2$ species lays 70.61 kcal/mol below the starting reactants. Among the studied final products, **11f′** is preferably obtained, from both a thermodynamic and a kinetic point of view: it is the most stable species, and the energetic barriers that have to be surmounted are smaller in the case of the O2-radical route. However, all the stationary points found for both the O1 and O2 radical routes are calculated to lay under the energy of the separated reactants, and hence, the outcome of the artemisinin decomposition products is predicted to depend mainly on the experimental conditions. The calculation results suggest that it is possible to find any of the three final products, as is experimentally confirmed.[21,22]

The chemical changes that take place in this reaction step involve O1−C4 bond formation simultaneously with O1−Fe bond breaking. As can be seen in Figure 7, the O1 and C4 atoms are 2.72 Å far from each other at **6f′**, while they are closer at **TS6f′-11f** (2.02 Å) and they are linked at **11f**, with a bond length of 1.45 Å. At **11f′**, this distance is 1.43 Å. The O1−Fe distance is 1.83 Å in **6f′** and evolves to 2.00 Å in **TS6f′-11f** and to 2.20 Å in **11f**, where the iron atom is still coordinated to O1.

The ELF analysis (Figure 8) reveals the existence of a disynaptic basin between the O1 and Fe cores in **6f′**, which is populated with 6.10 electrons and makes the bonding apparent. In **TS6f′-11f**, the disynaptic basin between these atoms has a population of 2.66 electrons, and a monosynaptic basin of 3.25 electrons appears that is constituted by the unshared electron pairs of O1. This means that the O1−Fe bond weakens at the transition state. In the product **11f**, there is no O1−Fe link, since no disynaptic basin has been found between these atoms. The C-radical character in **6f′** is demonstrated by the disynaptic basin located between C4 and Fe, which shows that the excess of charge is in this region and that C4 is coordinated to the Fe atom. In the transition state and **11f**, this basin is not present. The bond between O1 and C4 is evidenced by the disynaptic
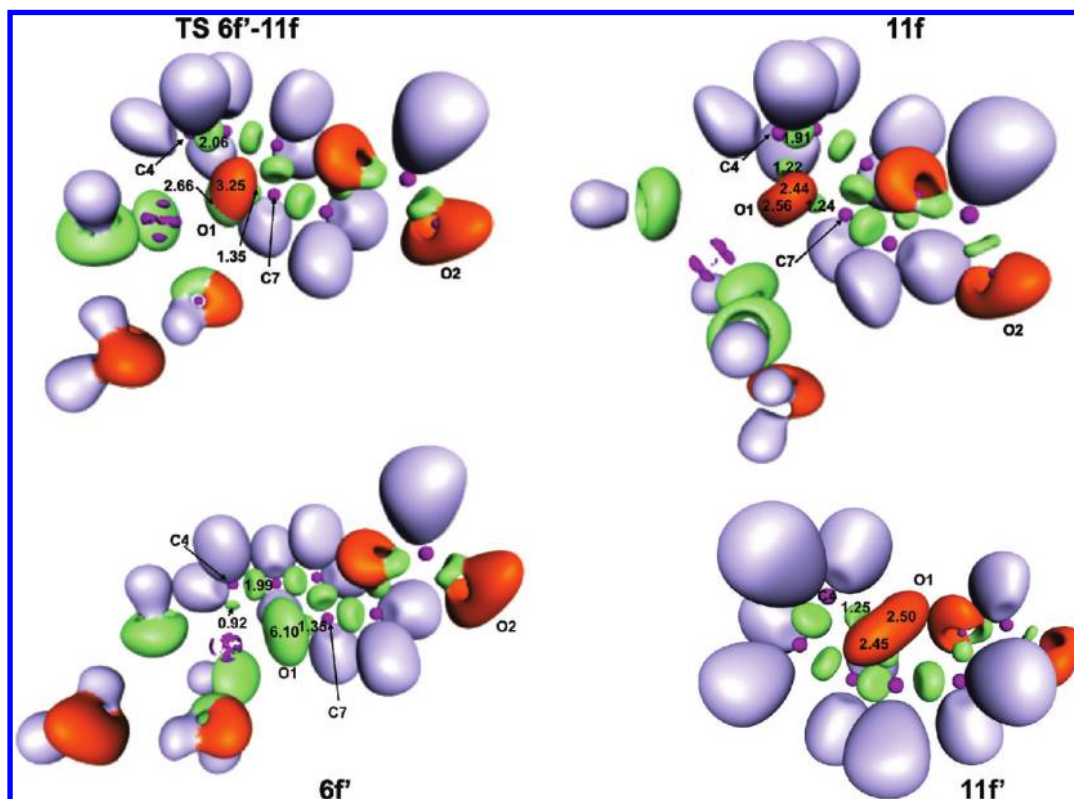
Late Steps of Artemisinin Decomposition

J. Phys. Chem. B, Vol. 115, No. 2, 2011 **345**

Figure 8. ELF isosurfaces for **6f′**, **TS6f′-11f**, **11f**, and **11f′**.

basin, populated with 1.22 electrons, which appears in **11f** between these atoms, being 1.25 electrons at **11f′**.

The spin density depicted in Figure 4d for **6f′** shows that the spin accumulates at C4, according to the C4 radical character of the molecule, and also accumulates at the Fe and its coordination sphere. At **TS6f′-11f**, the C4 radical character can still be viewed, because the TS has an early character with respect the C4−O1 bond formation. As for the MO, the HOMO of the TS accounts for the residual C4 radical character, while at **6f′**, it is the HOMO-1 which can accommodate the unpaired electron on C4, although the Fe−O1 interaction is also described by this orbital. The HOMO of **6f′** is mainly associated with a O1 p-type orbital.

The AIM theory describes the Fe−O1 bond scission with $\rho(r)$ values of 0.130 au in **6f′**, 0.082 au in **TS6f′-11f**, and 0.047 au in **11f**. $E_d(r)$ of this BCP has the value of −0.032 au in **6f′**, −0.006 au in the transition state, and 0.001 au in **11f**. $\nabla^2\rho(r)$ values (0.654 au in **6f′**, 0.422 au in **TS6f′-11f**, and 0.256 au in **11f**) show that the BCP is located in a charge depletion region for the three molecules. The same behavior was observed for the O2−Fe bond in the reaction which renders **7f** from **5f′**. This is attributed to the ionic character of the Fe−O bond. A BCP between C4 and O1 atoms appears in **TS6f′-11f**, with a $\rho(r)$ of 0.071 au, which evolves to 0.231 au in **11f** and to 0.249 at **11f′**. Also, $E_d(r)$ has the value of −0.010 au in **TS6f′-11f**, −0.285 au in **11f**, and −0.317 au in **11f′**. $\nabla^2\rho(r)$ values show that the BCP is in a charge depletion region in **TS6f′-11f** (0.129 au), while it is in a charge accumulation region in **11f** (−0.358 au) as well as in **11f′** (−0.470 au). From these results, the C4−O1 bond formation is demonstrated, as well as the fact that O1 still remains coordinated to the Fe atom at **11f**. As the BCP located between these atoms shows, the C4−O1 bond is slightly stronger in **11f′** than in **11f** due to the nonexistence of the Fe−O1 interaction in the first case.

Conclusions

The present work can be considered as the logical continuation of our previous work[20] and focuses on the geometric, energetic, and topological aspects of the steps leading from the C-radical species formed in the artemisinin decomposition process to the finally obtained products when heme alkylation fails. The analysis of the electron localization function (ELF) of Becke and Edgecombe[38] allows us to set up a mathematical model, which enables the study of the chemical structure of molecules, bringing a deep insight into the bond and lone pair localization. This description of the bonding has been used to study its evolution during a reactive process.

The obtained results nicely agree with the experimental data, and can shed additional light on our current understanding of the antimalarial action of artemisinin and its derivatives.

Some specific conclusions can be obtained from the present work: (a) The outcome of the experimentally detected products in the artemisinin decomposition process, namely, **8**, **10**, and **11**, has been satisfactorily explained. (b) The formation of **11f**, the model for **11**, has been found as the most favorable from a thermodynamic as well as a kinetic point of view, in agreement with the different experimental studies on the artemisinin decomposition process, that have found **11** as one of the main products.[21] (c) However, once the decomposition has been initiated, the formation of **8f** and **10f** is also possible according to the energetic profiles obtained. This agrees with the fact that **8** and **10** have also been detected, and our results explain that the product distribution will mainly depend on the experimental conditions. (d) The obtained energetic profiles also predict some accumulation of the intermediate **7f′**. This is experimentally confirmed by the detection of **7** in some experiments in small quantities.[21] (e) A new mechanistic proposal explaining the experimentally determined outcome of deoxiartemisinin **10** has been postulated. This alternative path would avoid the passage

through the species modeling **9**, and this would explain why such a species has never been experimentally identified. The fact that the highest-energy TSs in the path to **10f** and in the path to **8f** have energy values very similar to each other suggests some competition between the two pathways, and in fact from the experimental data, it is deduced that the predominant formation of **8** or **10** depends mainly on the experimental conditions. (f) The ELF analysis accurately describes the electron flows that lead from the C-centered radicals to the final products. Furthermore, the AIM study quantitatively accounts for the cleavage/formation of the bonds, and provides us with a picture at an electronic level of the chemical rearrangements taking place in the processes herein studied. The MO analysis together with the spin density description have also been used, providing additional direct evidence for the location of the radicals during the reaction steps. (g) By using **2**-H_2O, we have established the appropriateness of the use of **2f** to represent heme, because the energetic, geometric, and electronic conclusions reached are the same in both cases. Therefore, we use the small model, because it makes it possible to conduct high-level calculations and to perform the systematic topological analysis reported herein.

References and Notes

(1) Greenwood, B. M.; Fidock, D. A.; Kyle, D. E.; Kappe, S. H. I.; Alonso, P. L.; Collins, F. H.; Duffy, P. E. *J. Clin. Invest.* **2008**, *118*, 1266.

(2) Pereira, M. S. C.; Kiralj, R.; Ferreira, M. M. C. *J. Chem. Inf. Model.* **2008**, *48*, 85.

(3) Egan, T. J. *Mol. Biochem. Parasitol.* **2008**, *157*, 127.

(4) Zhang, S.; Gerhard, G. S. *PLoS One* **2009**, *4*, e7472.

(5) Kannan, R.; Kumar, K.; Sahal, D.; Kukreti, S.; Chauhan, V. S. *Biochem. J.* **2005**, *385*, 409.

(6) Rathore, D.; Jani, D.; Nagarkatti, R.; Kumar, S. *Drug Discovery Today: Therapeutic Strategies* **2006**, *3*, 153.

(7) Egan, T. J.; Combrinck, J. M.; Egan, J.; Hearne, G. R.; Marques, H. M.; Ntenteni, S.; Sewell, B. T.; Smith, P. J.; Taylor, D.; van Schalkwyk, D. A.; Walden, J. C. *Biochem. J.* **2002**, *365*, 343.

(8) Ginsburg, H.; Ward, S. A.; Bray, P. G. *Parasitol. Today* **1999**, *15*, 357.

(9) White, N. J. *Science* **2008**, *320*, 330.

(10) Meshnick, S. R.; Taylor, T. E.; Kamchonwongpaisan, S. *Microbiol. Rev.* **1996**, *60*, 301.

(11) Gu, J.; Chen, K.; Jiang, H.; Leszczynski, J. *J. Phys. Chem. A* **1999**, *103*, 9364.

(12) Taranto, A. G.; Carneiro, J. W.; d, M.; de Oliveira, F. G.; de Araujo, M. T.; Correa, C. R. *J. Mol. Struct. THEOCHEM* **2002**, *580*, 207.

(13) Robert, A.; Dechy-Cabaret, O.; Cazelles, J.; Meunier, B. *Acc. Chem. Res.* **2002**, *35*, 167.

(14) O'Neill, P. M.; Posner, G. H. *J. Med. Chem.* **2004**, *47*, 2945.

(15) Robert, A.; Benoit-Vical, F.; Claparols, C.; Meunier, B. *Proc. Natl. Acad. Sci. U.S.A.* **2005**, *102*, 13676.

(16) Tang, Y.; Dong, Y.; Wang, X.; Sriraghavan, K.; Wood, J. K.; Vennerstrom, J. L. *J. Org. Chem.* **2005**, *70*, 5103.

(17) Messori, L.; Gabbiani, C.; Casini, A.; Siragusa, M.; Vincieri, F. F.; Bilia, A. R. *Bioorg. Med. Chem.* **2006**, *14*, 2972.

(18) Golenser, J.; Waknine, J. H.; Krugliak, M.; Hunt, N. H.; Grau, G. E. *Int. J. Parasitol.* **2006**, *36*, 1427.

(19) Robert, A.; Bonduelle, C.; Laurent, S. A.-L.; Meunier, B. *J. Phys. Org. Chem.* **2006**, *19*, 562.

(20) Moles, P.; Oliva, M.; Sánchez-González, A.; Safont, V. S. *J. Phys. Chem. B* **2010**, *114*, 1163.

(21) Wu, W.-M.; Wu, Y.; Wu, Y.-L.; Yao, Z.-J.; Zhou, C.-M.; Li, Y.; Shan, F. *J. Am. Chem. Soc.* **1998**, *120*, 3316.

(22) Posner, G. H.; Cumming, J. N.; Ploypradith, P.; Oh, C. H. *J. Am. Chem. Soc.* **1995**, *117*, 5885.

(23) Cumming, J. N.; Ploypradith, P.; Posner, G. H. *Adv. Pharmacol.* **1996**, *37*, 253.

(24) McIver, J. W., Jr. *Acc. Chem. Res.* **1974**, *7*, 72.

(25) Fukui, K. *J. Phys. Chem.* **1970**, *74*, 4161.

(26) Frisch, M. J.; Trucks, G. W.; Schlegel, H. B.; Scuseria, G. E.; Robb, M. A.; Cheeseman, J. R.; Montgomery, J., J. A.; Vreven, T.; Kudin, K. N.; Burant, J. C.; Millam, J. M.; Iyengar, S. S.; Tomasi, J.; Barone, V.; Mennucci, B.; Cossi, M.; Scalmani, G.; Rega, N.; Petersson, G. A.; Nakatsuji, H.; Hada, M.; Ehara, M.; Toyota, K.; Fukuda, R.; Hasegawa, J.; Ishida, M.; Nakajima, T.; Honda, Y.; Kitao, O.; Nakai, H.; Klene, M.; Li, X.; Knox, J. E.; Hratchian, H. P.; Cross, J. B.; Bakken, V.; Adamo, C.; Jaramillo, J.; Gomperts, R.; Stratmann, R. E.; Yazyev, O.; Austin, A. J.; Cammi, R.; Pomelli, C.; Ochterski, J. W.; Ayala, P. Y.; Morokuma, K.; Voth, G. A.; Salvador, P.; Dannenberg, J. J.; Zakrzewski, V. G.; Dapprich, S.; Daniels, A. D.; Strain, M. C.; Farkas, O.; Malick, D. K.; Rabuck, A. D.; Raghavachari, K.; Foresman, J. B.; Ortiz, J. V.; Cui, Q.; Baboul, A. G.; Clifford, S.; Cioslowski, J.; Stefanov, B. B.; Liu, G.; Liashenko, A.; Piskorz, P.; Komaromi, I.; Martin, R. L.; Fox, D. J.; Keith, T.; Al-Laham, M. A.; Peng, C. Y.; Nanayakkara, A.; Challacombe, M.; Gill, P. M. W.; Johnson, B.; Chen, W.; Wong, M. W.; Gonzalez, C.; Pople, J. A. *Gaussian 03*; rev B.04; Gaussian, Inc.: Wallingford, CT, 2004.

(27) Becke, A. D. *J. Chem. Phys.* **1993**, *98*, 1372.

(28) Lee, C. T.; Yang, W. T.; Parr, R. G. *Phys. Rev. B* **1988**, *37*, 785.

(29) Silvi, B.; Savin, A. *Nature* **1994**, *371*, 683.

(30) Bader, R. F. W. *Atoms in Molecules: A Quantum Theory*; Oxford University Press: New York, 1990.

(31) Bader, R. F. W. *Chem. Rev.* **1991**, *91*, 893.

(32) Biegler-Konig, F.; Schonbohm, J.; Bayles, D. *J. Comput. Chem.* **2001**, *22*, 545.

(33) Noury, S.; Krokidis, X.; Fuster, F.; Silvi, B. *ToPMoD; Laboratoire de Chimie Théorique*; Université Pierre et Marie Curie: Paris, 1999.

(34) Konrad-Zuse-Zentrum, B., and Mercury Computer Systems *Amira 4.1*,1995-2006.

(35) *GaussView 3.0.*; Gaussian, Inc.: Wallingford, CT, 2003.

(36) Moles, P.; Oliva, M.; Safont, V. S. *J. Phys. Chem. A* **2006**, *110*, 7144.

(37) Moles, P.; Oliva, M.; Safont, V. S. *Tetrahedron* **2008**, *64*, 9448.

(38) Becke, A. D.; Edgecombe, K. E. *J. Chem. Phys.* **1990**, *92*, 5397.